

This is a self-archived version of an original article. This version may differ from the original in pagination and typographic details.

Author(s): Lehtivuori, Heli; Rumfeldt, Jessica; Mustalahti, Satu; Kurkinen, Sami; Takala, Heikki

Title: Conserved histidine and tyrosine determine spectral responses through the water network in *Deinococcus radiodurans* phytochrome

Year: 2022

Version: Published version

Copyright: © The Author(s) 2022

Rights: CC BY 4.0

Rights url: <https://creativecommons.org/licenses/by/4.0/>

Please cite the original version:

Lehtivuori, H., Rumfeldt, J., Mustalahti, S., Kurkinen, S., & Takala, H. (2022). Conserved histidine and tyrosine determine spectral responses through the water network in *Deinococcus radiodurans* phytochrome. *Photochemical and Photobiological Sciences*, 21(11), 1975-1989. <https://doi.org/10.1007/s43630-022-00272-6>



Conserved histidine and tyrosine determine spectral responses through the water network in *Deinococcus radiodurans* phytochrome

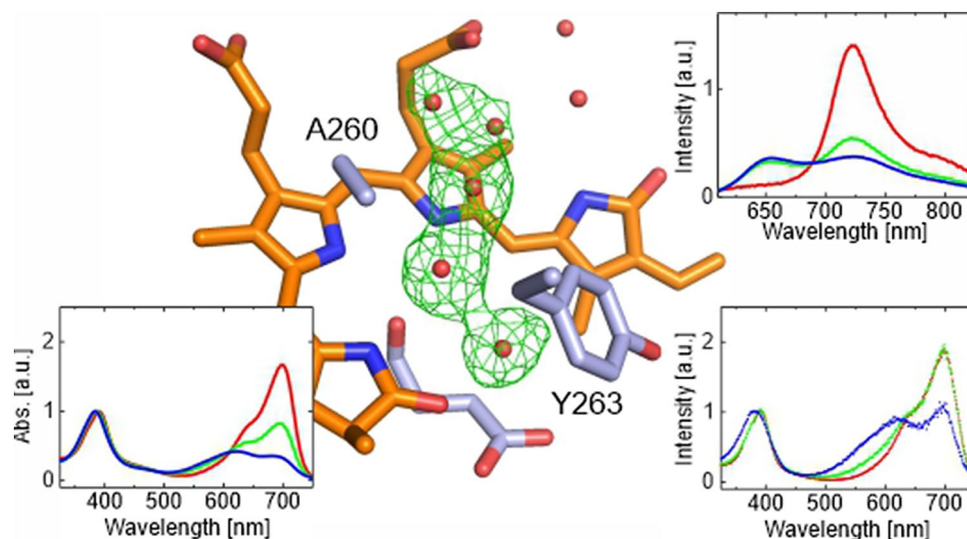
Heli Lehtivuori^{1,2} · Jessica Rumfeldt³ · Satu Mustalahti⁴ · Sami Kurkinen^{3,5} · Heikki Takala^{3,6}

Received: 29 April 2022 / Accepted: 12 July 2022
© The Author(s) 2022

Abstract

Phytochromes are red light-sensing photoreceptor proteins that bind a bilin chromophore. Here, we investigate the role of a conserved histidine (H260) and tyrosine (Y263) in the chromophore-binding domain (CBD) of *Deinococcus radiodurans* phytochrome (*DrBphP*). Using crystallography, we show that in the H260A variant, the missing imidazole side chain leads to increased water content in the binding pocket. On the other hand, Y263F mutation reduces the water occupancy around the chromophore. Together, these changes in water coordination alter the protonation and spectroscopic properties of the biliverdin. These results pinpoint the importance of this conserved histidine and tyrosine, and the related water network, for the function and applications of phytochromes.

Graphical abstract



Keywords Spectral responses · Water network · Biliverdin protonation · Phytochrome structure

This publication is dedicated to Prof. Silvia E. Braslavsky, a pioneer in photobiology and photobiophysics, on the occasion of her 80th birthday.

✉ Heikki Takala
heikki.p.takala@jyu.fi

Extended author information available on the last page of the article

1 Introduction

Phytochromes are red light-sensing photoreceptors originally discovered in plants [1] but can also be found in bacteria and fungi [2]. They bind a linear tetrapyrrole (bilin) chromophore and cycle between a red light-absorbing Pr state and a far-red light-absorbing Pfr state in response to

red/far-red irradiation [3]. Like many other photoreceptors, phytochromes consist of a photosensory module and an effector module. The photosensory module consists of a PAS (Per-ARNT-Sim), a GAF (cGMP phosphodiesterase-adenylate cyclase FhlA), and a PHY (phytochrome-specific) domain. In bacteriophytochromes, a biliverdin (BV) chromophore is covalently bound to a conserved cysteine in the PAS domain but physically embedded within the GAF domain (Fig. 1A). This PAS-GAF entity is often referred to as a chromophore-binding domain (CBD) [4]. As demonstrated first for a model bacteriophytochrome from *Deinococcus radiodurans* (*DrBphP*), red/far-red light induces large structural changes in the PSM [5]. These changes are then relayed to the effector module, regulating its activity [6, 7].

The photoreactions of bacteriophytochromes start with the photon absorption by the BV. Upon light absorption, phytochrome converts to the Pfr state, which absorbs far-red light ($\lambda \approx 750$ nm). This Pr-to-Pfr transition requires both CBD and PHY domain [8], has several intermediate states, and involves *Z*-to-*E* isomerization of the biliverdin D-ring with concomitant rotation of the C15-C16 methine bridge between the C- and D-ring [9–11]. The intermediate states include Lumi- and Meta-states; their kinetic and structural properties differ slightly between phytochrome species. The yield of reaching the first intermediate state, Lumi-R, is relatively low (< 15%) [12–17], and alternative reaction pathways, such as fluorescence and non-radiative relaxation (Fig. 1B), are generally competitive.

The intricate network of interactions formed by amino acid side chains and water molecules in the chromophore-binding pocket plays an important role in guiding the

photoresponses of the BV (Fig. 1A). For example, residues D207, H260, Y263, and H290 (numbering according to *DrBphP*) have been shown to play a role in the spectral fine-tuning of the photoresponses. In particular, D207 and Y263 play a critical role in the normal photocycle [19–21]. The two histidines, H260 and H290, are conserved in phytochromes and are centrally involved in the Pr-state structural heterogeneity [10, 22–26]. In addition, H260 is closely associated with the chromophore, placing its imidazole ring along with the inner pyrrole rings B and C.

The most central water molecule in the pocket, called pyrrole water (W1 in Fig. 1A), is coordinated between D207, H260, and the pyrrole nitrogens of the BV. It has been shown that initial photoreactions include its structural de-localization, accompanied by additional structural rearrangements about the chromophore [27]. Although the positions of several other coordinated waters in the chromophore-binding pocket are highly conserved in phytochromes, their role remains poorly understood. Lenngren et al. have shown that replacement of H290 side chain with threonine paves a way for two additional waters that affect the spectral responses of the BV [28]. In addition, Kraskov et al. have noticed that the histidine/threonine-dependent structural differences mainly refer to hydrogen bonding interactions with the ring D carbonyl group and, as a consequence, the torsion of the C–D methine bridge [26]. The water content in the vicinity of the chromophore has been traditionally linked to reduced fluorescence as the water network promotes vibrational relaxation pathways [29–31].

During the last decades, much effort has been made to modify the fluorescent properties of microbial fluorescent

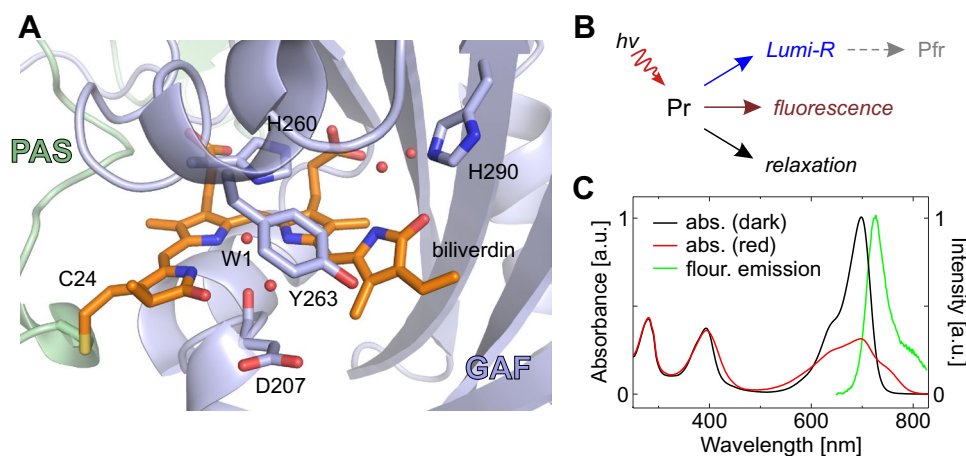


Fig. 1 Structure and photocycle of phytochromes. **A** Chromophore-binding pocket structure in wild-type CBD (CBD-WT) of *DrBphP*, PDB code 5K5B [18]. Biliverdin (orange sticks), key residues (blue sticks), and the pyrrole water (W1, red sphere) are indicated. **B** Three alternative reaction pathways induced by red light. Bacteriophytochrome can enter the photocycle via Lumi-R state. Alternatively, its biliverdin can emit a photon (fluorescence) or relax

to the ground state by other means (e.g., through vibrations or heat). **C** Normalized absorption and fluorescence spectra of a wild-type CBD fragment from *D. radiodurans* phytochrome. For absorption spectra, the sample was illuminated either with 785 nm light (“dark”) or 655 nm light (“red”) and normalized to the maximum of “dark” data. Emission spectrum was excited at 550 nm and normalized to its maximum. All spectra were measured at pH 8.0

protein markers from *DrBphP* [31–35], and phytochromes from *Rhodospseudomonas palustris* [36–39] and cyanobacteria [40–42]. Fluorescent phytochromes are a rapidly increasing area of current bioimaging research and will have an enormous impact on biological imaging strategies [43]. The wild-type CBD (CBD-WT) from *DrBphP* has a low fluorescence quantum yield (QY) of $(3.5 \pm 0.5)\%$ at pH 7.0 [44]. To improve this, protein modifications have been made to slow competing processes that occur after excitation, in particular non-radiative relaxation (Fig. 1B). The challenge in this kind of development is that improving the fluorescence QY typically results in emission in the orange part of the spectrum (~ 690 nm). Yet in *DrBphP*, the fluorescence QY of CBD has been increased up to almost 10% by site-selective mutations, while still maintaining the emission maximum at around 720 nm [31, 35].

In prototypical bacteriophytochromes, the absorption spectrum of the resting Pr state has two bands at around 400 nm (Soret band) and 700 nm (Q band) due to the covalently bound bilin chromophore (Fig. 1C). Experimental and theoretical studies indicate that in most phytochromes, the bilin chromophore exists in the fully protonated form at physiological pH. In this form, each of the four pyrrole nitrogens binds one hydrogen giving the molecule an overall positive charge [45–49]. The protonation state of bilin has been shown to influence its spectroscopic properties significantly [9, 23, 50–52]. As the pH increases, one hydrogen is released, most likely from the C-ring, which reduces the absorbance of the Q band [53]. Light- and X-ray-induced deprotonation of the C-ring has also been observed [47] reinforcing the notion that one of the pyrrole protons is labile.

In this study, we concentrate on the CBD fragment of *DrBphP*. We reveal how H260 together with Y263, plays an important role in the phytochrome photoresponses and protonation in the CBD. The crystal structures of the H260A and H260A/Y263F variants reveal that removal of the imidazole side chain clears the way for additional water molecules in the chromophore-binding pocket. The water network plays an important role in determining the spectral responses and (de)protonation events of the BV.

2 Results

To study the role of residues H260 and Y263 in the structure and photoresponses, we generated variants of the CBD fragment of *DrBphP* by site-directed mutagenesis. For H260, we chose alanine mutation (H260A), enabling a small non-polar substitution that is in close proximity to the four pyrrole nitrogens of the BV and the highly coordinated pyrrole water. As for Y263, we removed its hydroxyl group with Y263F mutation [21]. As a result, we ended up having a set of four CBD variants for our studies: wild-type CBD

(CBD-WT), CBD-Y263F, CBD-H260A, and CBD-H260A/Y263F.

2.1 H260 imidazole and Y263 hydroxyl affect the water content of the pocket

To assess the structural features in the chromophore vicinity caused by the mutations, we solved the crystal structures of CBD-H260A and CBD-H260A/Y273F. For crystallizing the variants, the same conditions were used as previously reported for CBD-WT and CBD-Y263F [18, 21]. The use of identical crystallization conditions enabled a direct comparison of all four variant structures. The H260A variants appeared to have reduced tendency to crystallize, which may indicate that they are structurally less stable than the CBD-WT and CBD-Y263F. The CBD-H260A and CBD-H260A/Y263F variants diffracted up to 1.88 Å and 1.48 Å, respectively (Table 3), and the overall structures were highly similar to the CBD-WT and CBD-Y263F. The rmsd values relative to CBD-WT were 0.13 Å for CBD-Y263F (8/317 residues rejected), 0.15 Å for CBD-H260A (14/314), and 0.18 Å for CBD-H260A/Y263F (15/315). The BV orientation was highly similar among the variants, and no differences were detected within the limits of the resolution (Supplementary Fig. 1). Most significant differences between the structures resided in the vicinity of the mutated residues at the chromophore-binding pocket.

Direct comparison of all four crystal structures (CBD-WT, CBD-Y263F, CBD-H260A, and CBD-H260A/Y263F) is shown in Fig. 2. All CBD variants contain a pyrrole water (W1), and a weaker density indicating a second water between the pyrrole water and the phenyl group of residue 263 (W2). However, in CBD-Y263F, this water density is weak, concurrent with the closer position of F263 to the pyrrole water. The chromophore-binding pockets of these CBD variants, including the coordinated waters, are very similar to the CBD-PHY fragment, except for the PHY tongue extension that binds to the pocket vicinity (see Supplementary Fig. 1C). In the CBD-H260A and CBD-H260A/Y263F, the removal of the histidine side chain however allowed 2–3 additional water molecules (W3 and W4) to occupy the positions of imidazole nitrogens (Fig. 2C, D). In addition, the electron density supports a fifth water molecule near W4 (W5), but its proximity to W4 (2.1 Å) and weak density indicate that this may be either an alternative position for W4 or a transient water. Waters W4 and W5 were therefore modeled with partial occupancy.

The lack of the histidine side chain and the involvement of additional waters also changed the hydrogen bonding network in the H260A variants (Fig. 2E, F). In CBD-WT and CBD-Y263F, the imidazole hydrogens of H260 interact with the pyrrole water and C-ring propionate. In H260A variants, these imidazole interactions are replaced by hydrogen bonds

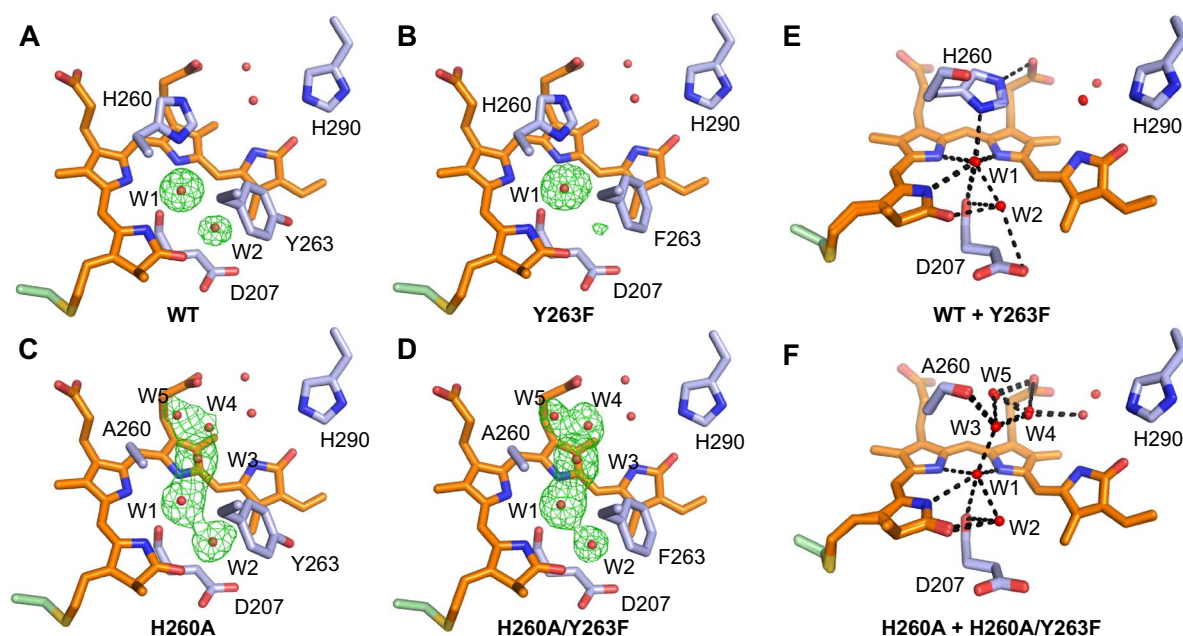


Fig. 2 Crystal structures and comparison of CBD variants. **A–D** Water omit maps at biliverdin surroundings of the four CBD variants: **A** CBD-WT [18], **B** CBD-Y263F [21], **C** CBD-H260A, and **D** CBD-H260A/Y263F. All variants contain a pyrrole water (W1) and usually a water between it and the residue 263 (W2). The variants containing the H260A mutation have extra space created by the missing imidazole side chain, which is occupied by additional water molecules (W3–W5). The Fo-Fc omit map (green mesh) is shown

at 4.0 rmsd. The maps were calculated by repeating the final step of each refinement without waters W1–W5. See [18] and [21] for refinement details of CBD-WT and CBD-Y263F, respectively. **E–F** Interactions of the waters W1–W5 in the biliverdin-binding pocket. These selected interactions are shown as black dashed lines. CBD-WT and CBD-Y263F are overlaid in panel E, whereas CBD-H260A and CBD-H260A/Y263F are overlaid in panel F

between W3 and A260 main chain hydroxyl, and W4 and C-ring propionate. Overall, the amount of hydrogen bonds in H260A variants has increased considerably.

2.2 Water coordination in the binding pocket directs the entrance to reaction pathway

The two mutations, H260A and Y263F, had striking effects on the water network in the chromophore-binding pocket (Fig. 2). To study the effects of these mutations on the initial photoreactions (Fig. 1B), time-resolved absorption and fluorescence measurements were conducted. We concentrated on the wild-type CBD and its single mutations (H260A and Y263F) to pinpoint the separate effect of these residues on the photocycle. The measurements were conducted at pH 8.0, like in other similar experiments [13, 14, 54]. The time-resolved absorption and fluorescence spectroscopy studies of CBD-PHY under similar conditions are published elsewhere [14, 21].

We used time-resolved absorption spectroscopy (pump-probe) from a femtosecond to nanosecond time scale to monitor the relaxation processes of the photoexcited samples. Pump-probe measurements for all samples were done by exciting the BV at 700 nm and monitoring in the

spectral range of 530–770 nm. For the spectra, see Supplementary Fig. 2. At a fast time scale, one can recognize ground state bleaching of the Q band together with stimulated emission. At a long time scale, an induced absorption at 730 nm appears, which can be assigned to Lumi-R state formation [13]. In Fig. 3A, we show trace curves at 730 nm with their fits for CBD-WT, CBD-H260A and CBD-Y263F. Typically, multi-exponential data fitting is used to analyze the time-resolved absorption traces, and this approach was required for all CBD variants in this study. The parameters are summarized in Table 1. Until 6 ns, the resulting transient absorption traces of CBD-WT show features that have been previously reported [14]. Only CBD-WT shows induced absorption at 730 nm typical of Lumi-R, whereas CBD-Y263F and CBD-H260A do not display this absorbance (Fig. 3A). This is consistent with our steady-state measurements at pH 8.0 (Supplementary Fig. 3A–C), and our published results with the Y263F variant [21], where only minor absorption at around 750 nm appeared in CBD-Y263F and CBD-H260A after illumination with red light. Despite this small absorption signal, urea denaturation experiments indicate, however, that BV isomerization occurs in illuminated CBD-H260A to a similar extent as in wild-type CBD and CBD-PHY fragments (Supplementary Fig. 3E–I).

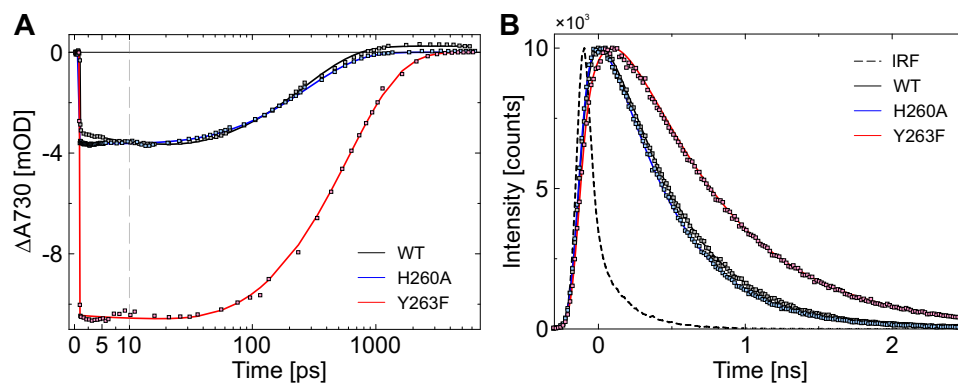


Fig. 3 Transient absorption and emission decays of three CBD variants. **A** Transient absorption traces of CBD-WT, CBD-H260A and CBD-Y263F at pH 8.0. Samples were excited at 700 nm and absorption was monitored at 730 nm. Solid lines show the multi-exponential

fit of the data. **B** Emission decays of CBD-WT, CBD-H260A and CBD-Y263F at pH 8.0. Samples were excited at 660 nm and emission was monitored at 720 nm. IRF is the instrument response function

Table 1 Time-resolved spectroscopic characteristics of the CBD-WT, CBD-Y263F, and CBD-H260A at pH 8.0. TCSPC stands for Time-Correlated Single-Photon Counting

Variant	TCSPC τ_{ave} (ps)	pump-probe τ_1 (ps)	pump-probe τ_2 (ps)	pump-probe τ_3 (ns)
CBD-WT	430 ± 30*	10 ± 5	380 ± 30	> 6
CBD-Y263F	670 ± 30*	27 ± 10	680 ± 30	–
CBD-H260A	420 ± 30*	16 ± 8	370 ± 30	–

*The average decay values of the two exponential decay components are presented for CBD-WT and CBD-H260A. In the case of CBD-Y263F, one component was applied

Isomerization of illuminated CBD-Y263F was only 23% of that observed for CBD-WT (Supplementary Fig. 3H).

The time-resolved fluorescence measurements of CBD-WT, CBD-H260A, and CBD-Y263F (Fig. 3B) demonstrate that the fluorescence lifetimes correlate well with the second time constants (τ_2) of pump-probe measurements (Table 1). The excitation decay properties of the BV in the binding pocket can be studied using 660 nm excitation and 720 nm monitoring wavelengths. Similar to previous time-resolved studies of phytochrome systems [35], the fluorescence decays were fitted with multi-exponential functions to obtain the excited-state lifetimes of the CBD variants. We found two categories: first category contained CBD-WT and CBD-H260A, whose decay profile required two exponential components. In the second category, a mono-exponential fit was sufficient to describe the fluorescence decay of CBD-Y263F. The average decay times were 430 ps (CBD-WT), 670 ps (CBD-Y263F), and 420 ps (CBD-H260A).

2.3 UV-Vis absorption of pH titrations in the Pr state show two distinct BV protonation states

The time-resolved measurements indicated that the water content in CBD variants affect the fluorescence properties and the production of a Lumi-R-like state (Fig. 3). Previous

studies have shown that H260 and Y263 play a role in the BV protonation [50, 52]. For example, Y263F mutation in *DrBphP* CBD-PHY fragment increases the occurrence of a pH-dependent BV population that absorbs at 650 nm when deprotonated [52]. To study whether these results apply for the CBD fragment, we applied the same four variants for pH-dependent absorption spectroscopy (Fig. 4).

Similar to pH titrations of CBD-PHY fragment [52], an increase in pH led to a decreased absorption of the Q band centered at 700 nm, which has been attributed to deprotonation of the biliverdin chromophore [50, 55, 56]. The absorption at 700 nm as a function of pH is shown for each variant fit to a single pK_a model in Fig. 4E. For the CBD-WT and CBD-Y263F, the midpoint pH of the titration is greater than 10 (Fig. 4E), similar to the CBD-PHY counterparts [52]. Due to the protein instability at high pH values, the endpoint of the titration could not be measured and therefore accurate pK_a values determined. For CBD-H260A and CBD-H260A/Y263F, the lack of H260 imidazole decreases the midpoint of the pH titration by over two pH units. As a result, the approximate pK_a value was 7.6 for both CBD-H260A and CBD-H260A/Y263F, similar to the pK_a values of near 8 determined in their CBD-PHY counterparts [52]. Due to the above effects, the BV deprotonation starts to become significant at and above pH 9 in WT and Y263F. The absence

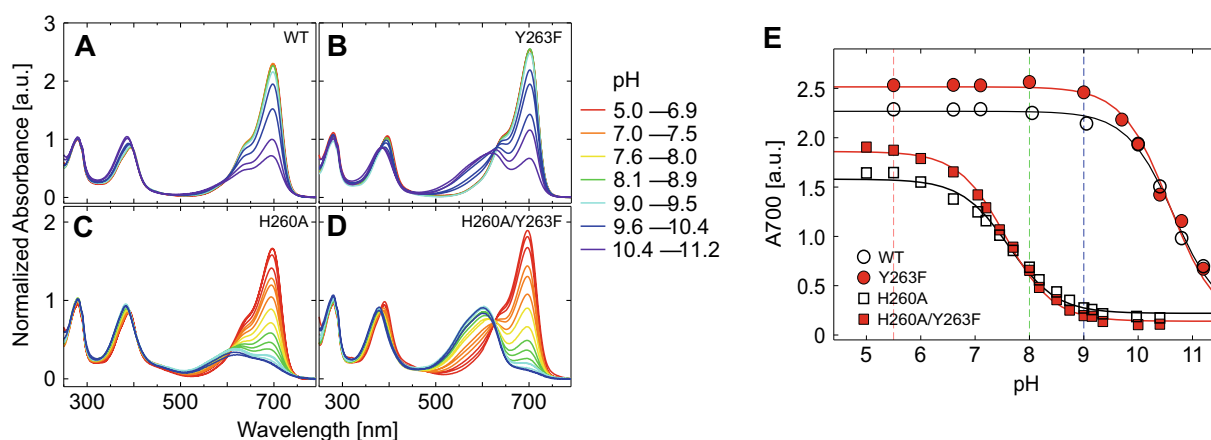


Fig. 4 Absorption spectra of CBD variants in the Pr state at different pH values. **A** CBD-WT, **B** CBD-Y263F, **C** CBD-H260A, and **D** CBD-H260A/Y263F. All spectra are color-coded according to the measured pH. **E** The absorbance value at 700 nm plotted as a function of pH for CBD variants. The solid lines represent the fit to a deprotonation model with one pK_a [52]. For WT and Y263F, the end-

point absorbance values at high pH were fixed to those obtained for H260A and H260A/Y263F, respectively, resulting in fitted pK_a values of 10.7 (WT) and 10.6 (Y263F). The fitted pK_a value for both H260A and H260A/Y263F is 7.6. The pH values selected for the following experiments (5.5, 8.0, and 9.0) are indicated as vertical dashed lines

of the PHY tongue, an extension of the PHY domain that shields the chromophore vicinity of CBD, does not notably affect the pK_a of the BV [52]. Previous studies with CBD-PHY fragment indicated a pH-induced deprotonation of the BV and the Y263 hydroxyl [52]. In CBD-H260A, the residuals from the fit to a single pK_a indicate some deviation from two-state behavior (see Supplementary Fig. 4), similar to CBD-PHY H260A variant. However, this deviation is also observed for CBD-H260A/Y263F, which does not have the hydroxyl group at position 263, thus providing no indication of Y263 deprotonation in CBD-H260A. Using singular value decomposition (SVD), two deprotonation events are observed for CBD-WT while only one is indicated for CBD-Y263F (Supplementary Fig. 5), which suggests Y263 deprotonation in CBD-WT. SVD also gives some indication for Y263 deprotonation in CBD-H260A, but not as clear as observed in CBD-PHY.

2.4 Fluorescence properties of the pH-dependent populations

The existence of the pH-dependent populations in the CBD variants (Fig. 4) led us to assume that these populations were also visible in the fluorescence spectra. We therefore continued to measure the absorption, fluorescence emission, and fluorescence excitation spectra at various pH values. We chose three specific pH values to cover different degrees of protonation of the H260 variants: greater than 99% protonated at pH 5.5, ~30% protonated at pH 8.0, and ~3% protonated at pH 9.0 (Fig. 4E). With CBD-WT and CBD-Y263F this trend is not as prominent, as BV remains at least 99.9% protonated at pH values 5.5 and 8.0, and approximately 98%

protonated at pH 9.0. The resulting spectra at three selected pH values are shown in Fig. 5, and all parameters are summarized in Table 2.

The shapes of the CBD-WT emission spectra (Fig. 5E) were similar at all pH values, consistent with the absorption measurements (Fig. 5A). However, a small blue-shift of 4 nm could be observed when increasing the pH, concomitant with the decrease of the fluorescence QY from 3.0% (pH 5.5) to 1.3% (pH 9.0). Compared to CBD-WT, the fluorescence emission of CBD-Y263F was less sensitive to changes in pH (Fig. 5F). The shape and the QY of the spectra remained almost unchanged between pH 5.5 and 8.0, and only a small additional emission peak appeared around 650 nm at pH 9.0. In CBD-H260A and CBD-H260/Y263F, the shape and intensity of the emission spectra however did not remain as constant at different pH values (Fig. 5G, H). Both variants had two emission maxima, at 650 nm and 722 nm. The 722 nm emission peak decreased abruptly with increasing pH. This decrease was accompanied by an increase of the 650 nm emission peak, which levels off at pH 8.0. These pH-induced changes in spectra are even more significant for the double variant, which shows a clear 651 nm peak already at the lowest pH value (pH 5.5) and a near disappearance of the 722 nm peak at the highest pH value (pH 9.0). As the fluorescence spectra of CBD-H260A and CBD-H260A/Y263F did not show PPIXa-specific emission peaks at 622 nm and 688 nm [44], we conclude that the entire emission profile originates from the BV molecules covalently bound to protein.

To demonstrate the fluorescence properties at 650 nm and 750 nm further, we measured the excitation spectra of the CBD variants detected at these two different wavelengths

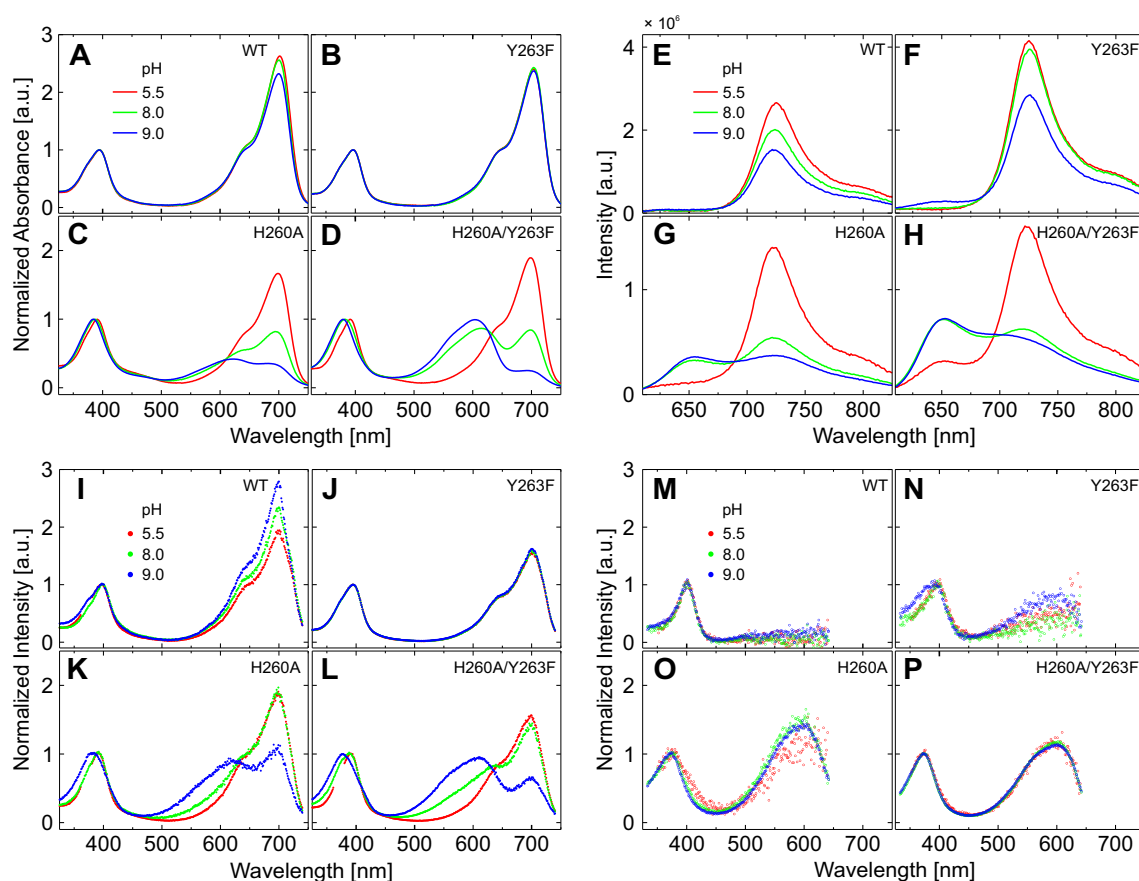


Fig. 5 Steady-state absorption, emission, and excitation spectra of the CBD variants at three different pH values: 5.5 (red), 8.0 (green) and 9.0 (blue). **A–D** Absorption spectra of WT (**A**), Y263F (**B**), H260A (**C**), and H260A/Y263F (**D**). The spectra were normalized at the Soret band (around 400 nm). **E–H** Emission spectra of WT (**E**), Y263F (**F**), H260A (**G**), and H260A/Y263F (**H**) excited at 550 nm. The fluorescence intensities were corrected for the num-

ber of absorbed photons. **I–L** Excitation spectra of WT (**I**), Y263F (**J**), H260A (**K**), and H260A/Y263F (**L**) at 750 nm emission. **M–P** Excitation spectra of WT (**M**), Y263F (**N**), H260A (**O**), and H260A/Y263F (**P**) at 650 nm emission. All excitation spectra are normalized at the Soret band (around 400 nm) and therefore the intensities are not directly comparable between the variants

Table 2 Steady-state spectroscopic characteristics of the CBD variants at three different pH values

Variant	pH	Abs. max (nm)	Q/Soret ratio	Exc. max (nm) at 650 nm emis.	Exc. max (nm) at 750 nm emis.	Q/Soret ratio at 750 nm emis.	Em. max (nm)	Φ_F (%) ^b
WT	5.5	700	2.8	–	700	2.0	723	4.2
	8.0	696	2.7	–	696	2.3	719	2.6
	9.0	696	2.4	–	696	2.8	719	1.7
Y263F	5.5	701	2.5	–	700	1.6	723	4.5
	8.0	701 ^a	2.5	–	700	1.6	723 ^a	4.2 ^a
	9.0	701	2.4	600	700	1.7	653 and 723	3.3
H260A	5.5	700	1.9	600	700	2.1	722	4.5
	8.0	697	1.0	600	700	2.1	653 and 722	1.1
	9.0	625 and 688	0.4	600	622 and 698	1.3	653 and 722	1.0
H260A/Y263F	5.5	698	2.1	600	700	1.8	651 and 722	4.1
	8.0	616 and 698	1.1	600	700	1.6	651 and 722	1.6
	9.0	606 and 696	0.4	600	612 and 700	0.9	651	1.4

^aAbsorbance and emission maxima and fluorescence quantum yield as reported in [33]

^bThe fluorescence quantum yields were determined at 550 nm

(Fig. 5I–P). The excitation spectra at 750 nm emission (Fig. 5I–L) showed that all variants have a component that absorbs at the Q band. The excitation spectra at 650 nm emission for CBD-WT and CBD-Y263F (Fig. 5M, N) had very similar shapes at almost every pH value, but the excitation spectrum for CBD-Y263F at pH 9.0 had a small broad peak at around 600 nm. This peak indicates a second fluorescent component with low 600 nm absorption. The excitation spectra of CBD-H260A and CBD-H260/Y263F confirm the existence of at least two fluorescing components. Their excitation spectra at 750 nm emission (Fig. 5K, L) show that the second component is present mainly at the highest pH values, and the excitation spectra at 650 nm emission (Fig. 5O, P) show that the second component absorbs widely at around 600 nm.

To aid comparison, the excitation and absorption spectra (Fig. 5A–D) are normalized to the maximum of the Soret band at approximately 400 nm. The overall similarity between the excitation spectra at 750 nm emission (Fig. 5I–L) and absorption spectra (Fig. 5A–D) for all variants, suggests that this part of the emission is due to normally oriented BV [22]. However, a closer inspection indicates that the ratios between the Q and Soret band intensities are different in absorption spectra and excitation spectra (Fig. 5 and Table 2). This is most clearly observed in CBD-Y263F and CBD-WT. The Q/Soret ratio for CBD-Y263F was lower in the excitation spectra than in the absorption spectra at all pH values. For CBD-WT, however, the ratio in the excitation spectra changes more significantly as a function of pH, being lower than in the absorption at pH 5.5 but higher at pH 9.0. This suggests that the excited-state energy surfaces, responsible for Q and Soret absorption, are similarly affected at pH 5.5 but differ as the pH increases. Since the pH titration in Fig. 4 indicates no significant deprotonation of BV, a logical candidate for these effects is deprotonation of the Y263 hydroxyl.

The H260A and H260A/Y263F variants can also be used to distinguish the effects of pH with and without the Y263 hydroxyl, although the interpretation is complicated by significant deprotonation of the BV. The Q/Soret ratio for CBD-H260/Y263F was lower in excitation spectra than absorption

spectra at pH 5.5 and higher at pH 8.0 and 9.0, whereas the ratio for CBD-H260A in excitation spectra was higher than absorption spectra at all pH values. Given that the pK_a values of these variants are similar, it suggests that Y263 hydroxyl is deprotonating. Y263 was also observed to deprotonate around pH 8.0 in pH titration experiments of CBD-PHY-WT and CBD-PHY-H260A [52]. In this study, SVD analysis indicates Y263 hydroxyl deprotonation for CBD-WT. However, the evidence is not as clear for deprotonation of this tyrosine in CBD-H260A (Supplementary Fig. 5). Possibly the non-two-state behavior observed in both CBD-H260A and CBD-H260A/Y263F (Supplementary Fig. 4) makes the detection of Y263 deprotonation difficult, as several pH-dependent processes seem to occur concurrently between pH 6 and 9.

3 Discussion

The available space, amount of water molecules, and the flexibility of the chromophore-binding pocket have been proposed as the main factors to explain the spectral behavior of phytochromes [31, 54, 57]. In this study, we have studied H260 and Y263 in the function of the CBD fragment of *D. radiodurans* phytochrome. Namely, we showed that these residues have an important role in the Pr state and water content of the chromophore-binding pocket. Through these waters, the residues influence the photoreaction pathway taken, by selectively favoring either Lumi-R state, fluorescence, or non-radiative relaxation pathway. We also showed that these residues protect BV against changes in solvent pH by excluding water molecules from the BV-binding pocket. The main conclusions are summarized in Fig. 6.

The initial steps in the photocycle of phytochromes, i.e., from the Pr state to the Lumi-R state, have been extensively studied by time-resolved absorption spectroscopy [13–15, 24, 54, 58–60]. The kinetics of the various BV-binding phytochrome photoreactions do not differ significantly. Mutational studies have identified highly conserved key amino acids, like Y263, D207, H260, and H290, in the immediate vicinity of the D-ring, which directly affect the excited-state

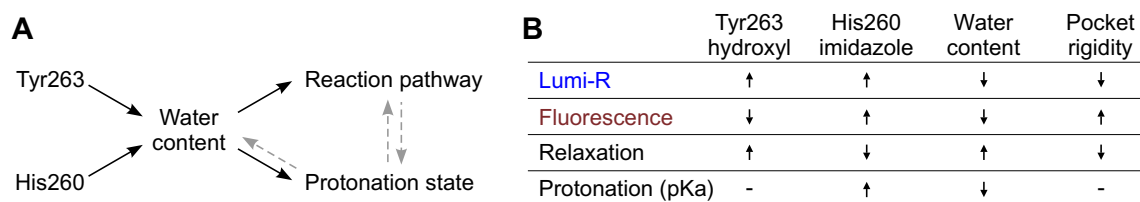


Fig. 6 Summary of the results obtained in the study. **A** Simplified scheme of the events related to the coordinated water content in the chromophore-binding pocket. H260 and Y263 affect the water network, which then affects the chosen reaction pathway (Lumi-R, fluo-

rescence, or non-radiative relaxation) and the protonation state of the biliverdin. Only relations through the coordinated waters within the pocket are shown. **B** The effects of H260, Y263, and pocket parameters on the photoreaction pathway taken and on the pK_a

lifetime and the isomerization quantum yield, as now observed for H260 and Y263 (Fig. 3).

One surprising finding with the H260A variant is that it does not seem to reach the Lumi-R state spectrally (Fig. 3A) even though its BV isomerizes (Supplementary Fig. 3I). There was also no rise of 730 nm absorbance typical of the Lumi or Meta state formation in this variant (Supplementary Fig. 3C), which indicates that light-induced BV isomerization does not lead to the typical structural changes in the chromophore-binding pocket. The crystal structure of CBD-H260A shows that the removal of the H260 side chain increases the water content of the chromophore pocket (Fig. 2C). These additional waters extend the hydrogen bonding network, therefore reducing the rigidity of the chromophore surroundings and potentially absorbing light-induced structural changes. Studies with serial femtosecond crystallography (SFX) indicate a pyrrole water re-localization (photo-ejection) within first picoseconds after photoexcitation [27, 61]. This initial water movement may be affected by the modified bonding network caused by the H260A mutation. The changes may increase the probability for non-radiative relaxation at the expense of other pathways (Fig. 6B). Indeed, one could also envision that removal of the H260 imidazole would hamper the structural framework of the 'normal' Lumi-R state with defined BV interactions [62]. In addition, the bathochromic shift in the Pr-to-Pfr photoconversion is proposed to be due to changes in the chromophore interactions with the surrounding pocket rather than isomerization [9–11]. This may also apply to the transition from the Pr state to the Lumi-R state.

The fluorescence of a molecule is extremely sensitive to local environmental changes. Although mutating H260 and Y263 had practically no effect on the orientation of BV (Supplementary Fig. 1), it had a large impact on the fluorescence properties of the CBD. Interestingly, the quantum yield of fluorescence is decreased in CBD-H260A when compared to CBD-WT, but the fluorescence lifetime is almost the same at pH 8.0 (Tables 1 and 2). We can therefore conclude that the increased hydrogen bonding in the H260A pocket appears as static fluorescence quenching [63]. In the case of Y263, both its interactions with the BV as well as its participation in the hydrogen bonding network have been proposed to be essential for efficient photochemistry [21]. For example, Toh and coworkers have demonstrated that increased H-bond strength to ring D increases excited-state lifetime and reduces the quantum yield of Lumi-R formation in *Rps. palustris* RpBphP3 and RpBphP2 [13]. Conversion of tyrosine to phenylalanine alters the interaction of the residue with water molecules since the polar phenol group is replaced with a benzyl group that interacts mainly through its π -electron system [21]. The benzyl group in Y263F interacts more closely with the D-ring, leading to decreased W2 occupancy (Fig. 2B). This reduced water content then may

play a role in increased fluorescence of the Y263F variant (Fig. 3B).

The additional waters in the H260A variants facilitate the proton exchange between the BV and the surrounding solution. Indeed, these waters form a channel in the chromophore-binding pocket, which is guarded by Y263 side chain (Fig. 2C, D). Both H260 and Y263 seem to play a role in BV (de)protonation through water content of the chromophore-binding pocket (Fig. 6A). Feliks et al. have studied *D. radiodurans* CBD and its IFP-derivatives at different pH values. They have shown in their molecular dynamics simulations that altering the protonation states of H260 leads to different patterns of interaction between water molecules and the chromophore-binding pocket [48], which further affects their spectroscopic properties. According to Rumfeldt et al. the pK_a value of the Y263 phenol in the canonical bacteriophytochromes is uncommonly low and this feature of Y263 directly influences protonation of the chromophore [52]. In addition, Sineshchekov et al. have hypothesized that this distinct property of Y263 contributes to the appearance of the two Cph1 species, probably differing by the degree of their protonation [64]. Comparison of the Q/Soret ratio in excitation vs. absorption spectra in CBD-WT and CBD-Y263F (Fig. 5) supports the results of SVD (Supplementary Fig. 5) that Y263 hydroxyl also deprotonates in CBD.

The CBD-PHY fragment of the DrBphP can enter the full photocycle [8] and has a PHY tongue extension that interacts with the GAF domain close to the chromophore-binding pocket. These features could affect the reaction pathways taken by the BV (Fig. 6). The PHY tongue may hinder the exchange of the water molecules with the BV-binding pocket but does not necessarily affect the content of its coordinated waters and thus fluorescence properties. Indeed, according to crystal structures of CBD and CBD-PHY (Supplementary Fig. 1C), the main difference in the water content lies outside the chromophore-binding pocket where the PHY tongue residues are replaced by solvent waters in CBD [5, 18, 20]. The pK_a of the biliverdin remains unchanged in CBD and CBD-PHY fragment titrations (Fig. 4 and [52]), which supports the notion that the imminent BV surroundings do not seem to be affected by the PHY tongue.

Our absorption and fluorescence measurements of CBD show that the mutations of H260 and Y263 have an increased population of species that absorb at 615 nm and emit at 653 nm (Fig. 5). The one that absorbs at 615 nm is clearly the deprotonated population and the one that absorbs closer to 700 nm is the protonated population similar to CBD-PHY fragment [52]. Indeed, the pH titrations of phytochromes combined with absorption spectroscopy have demonstrated, that at higher pH, the intensity of the Q band decreases, and the observed decrease was assigned to chromophore deprotonation [23, 50, 51]. In numerous spectroscopic studies, the blue-shifted shoulder of the Q band

(Fig. 1A) has been linked to the heterogeneity of the ground state in phytochromes [64–66], which is also supported by NMR and Resonance Raman spectroscopy [10, 67]. In some cases, phytochrome heterogeneity may be related to the different protonation states of the chromophore or of the highly conserved histidine (H260 in *DrBphP*) [10]. Our results show that the deprotonation of the BV leads to a broad peak at a maximum of 600 nm that differs from the Q band shoulder. Although having several protonation states may explain some of the heterogeneity, there are also other sources for this phenomenon. As the protonation state of each phytochrome sample depends on the prevalent pH value (Fig. 4), one should take the pH into careful consideration while studying phytochromes.

4 Experimental procedures

4.1 Cloning, protein expression and purification

The CBD fragment (amino acids 1–321) of *D. radiodurans* phytochrome and its CBD-Y263F variant are described elsewhere [4, 19, 21]. The H260A and H260A/Y263F mutations were introduced with QuikChange Lightning Multi Site-Directed Mutagenesis Kit (Agilent Technologies) as in [52]. The proteins were expressed and purified as described previously [21, 52]. After the final size-exclusion chromatography step, the purified protein samples in (30 mM Tris/HCl, pH 8.0) were concentrated to 25–30 mg/ml, flash-frozen with liquid nitrogen, and stored at $-80\text{ }^{\circ}\text{C}$.

4.2 Protein crystallography

The CBD-H260A and CBD-H260A/Y263F crystals were grown with similar conditions as in [18]. The hanging-drop vapor diffusion method was applied, in which 15 mg/ml protein was mixed at a 1:1 ratio with reservoir solution (67 mM sodium acetate, pH 4.95, 3.3% PEG 400, 10–25% 2-methyl-2,4-pentanediol, 1 mM DTT). The crystals were grown in the dark, in a cold room, and flash-frozen without additional cryo-protectants under green safe light. The diffraction data were collected with 0.968 Å wavelength in beamline ID30A-3 of the European Synchrotron Radiation Facility (ESRF). The data were processed with the XDS program package version June 1, 2017 [68]. The CBD-H260A data were cut at 1.88 Å resolution and the CBD-H260A/Y263F data at 1.48 Å, which corresponds to a correlation coefficient ($CC_{1/2}$) value of 0.33 and 0.38, respectively [69].

The crystal belonged to the C121 space group with cell parameters highly similar to wild-type CBD [18] and CBD-Y263F [21]. Both crystal structures were solved by molecular replacement with Phaser version 2.5.7 [70] and 2O9C [19] as a search model. The structures were further refined

with REFMAC5 version 5.8.0267 [71], with final refinement steps using 0.03 matrix weight and isotropic temperature factors for CBD-H260A and 0.1 matrix weight and anisotropic temperature factors for CBD-H260A/Y263F. The model building and real space refinement was conducted with Coot 0.9.6. The final structures had Rwork/Rfree values of 0.187/0.225 (CBD-H260A) and 0.128/0.169 (CBD-H260A/Y263F). The crystal data collection and processing statistics are summarized in Table 3.

The maps were calculated by repeating the final step of each refinement without waters W1–W5 (Fig. 5), and the structure figures were created with the PyMOL Molecular Graphics System version 2.5.2 (Schrödinger, LLC). The RMSD between CBD variants were calculated with PyMOL after outlier rejection.

4.3 Spectroscopic measurement

All measurements were carried out at room temperature in darkness. For measurement of samples in the Pr state, CBD variants were illuminated for 1 min with a 785 nm miniature diode laser (far-red, 250 mW output power). CBD variants were converted to the Pfr state by illuminating with a 655 nm (red, 7-milliwatt output power) light-emitting diode light until photoequilibrium was reached.

Steady-state absorption measurements: stock solutions of the phytochromes in the Pr state were diluted into solutions buffered between pH 5.0 and 11.0: Citrate buffer was used for pH 5.0 and 5.5, MES buffer was used for pH 6.0–7.1, Tris for pH 7.2–9.2, and glycine for pH 9.3–11.0. The final concentration of the buffer was 30 mM with constant ionic strength maintained at all pH values using NaCl. The final concentrations of CBD constructs were $\sim 4\text{ }\mu\text{M}$ giving a 700 nm absorbance of about 0.25 at pH 7.0.

Proteins in the Pr state or after illumination to photoequilibrium with 655 nm light were measured by absorption spectroscopy or were diluted into 10 M urea pH 3 for final urea concentration of 8.0 M. The CBD variants in urea were then measured by absorption spectroscopy within 1–2 min of urea denaturation.

Steady-state fluorescence measurements: steady-state fluorescence measurements were performed in three different pHs (5.5, 8.0 and 9.0). Each sample solution was prepared by dilution from a stock solution using citrate buffer for pH 5.5, Tris buffer for pH 8.0 and glycine buffer for pH 9.0. For fluorescence quantum yield measurements, samples were diluted into the appropriate buffer and filtered: one half of the sample was taken for fluorescence measurement and the other half for absorption. Steady-state absorption spectrum of the samples was measured to determine the concentration of the analyzed solutions. The samples used to record fluorescence were diluted to sufficiently low absorption values (between 2 and 10 μM to give OD_{700} of 0.1) to prevent

Table 3 Crystal data collection and processing statistics

Parameters	CBD-H260A	CBD-H260A/Y263F
Data Collection		
Space group	C121	C121
Cell dimensions		
<i>a</i> , <i>b</i> , <i>c</i> (Å)	93.93, 54.39, 70.47	93.76, 54.33, 70.37
α , β , γ (°)	90.00, 92.39, 90.00	90.00, 92.16, 90.00
Resolution (Å)	19.91–1.88 (1.93–1.88) ^a	19.84–1.48 (1.52–1.48) ^a
<i>R</i> _{merge}	0.145 (1.683)	0.041 (1.450)
<i>CC</i> _{1/2}	0.996 (0.324)	0.999 (0.383)
<i>I</i> / σ (<i>I</i>)	7.38 (0.67)	16.43 (1.05)
Completeness (%)	98.9 (97.1)	97.1 (95.9)
Redundancy	4.87 (4.64)	4.21 (4.33)
Wilson B factor	34.48	31.12
Refinement		
Resolution (Å)	19.91–1.88 (1.93–1.88) ^a	19.84–1.48 (1.52–1.48) ^a
No. of reflections	27,327 (1,936) ^a	54,489 (3,911) ^a
<i>R</i> _{work} / <i>R</i> _{free}	0.187/0.225 ^b (0.423/0.416)	0.128/0.169 ^b (0.466/0.510)
Overall B factor	36.50	30.70
No. of atoms		
Protein	2,352	2,351
Heterogen ^c	63	71
Water	265	373
Geometry		
RMSD		
Bond lengths (Å)	0.005	0.007
Bond angles (°)	1.343	1.448
Ramachandran		
Favored (%)	98	99
Allowed (%)	2	0
Outliers (%)	0	0
PDB Code	7Z9D	7Z9E

^aOuter shell values are in parentheses^bTest set for *R*_{free} calculation constitutes 5% of total reflections that were randomly chosen^cThis includes atoms from biliverdin, acetate and (4S)-2-methyl-2,4-pentanediol

an inner filter effect. Fluorescence spectra were measured with the Horiba Aqualog fluorometer. Emission spectrum of each sample was measured with two emission wavelengths 550 nm and 630 nm (1 s accumulation, 20 repeats, 2 pixels). The fluorescence quantum yield was determined from the steady-state absorption and emission spectra [31]. In addition, fluorescence excitation–emission matrix data were measured (0.2 s accumulation, 3 repeats, 2 pixels). 5 nm emission and excitation slits were used in all measurements.

Time-resolved absorption and fluorescence: to avoid excessive sample degradation, the sample solution (volume 400 μ L) was cycled using a peristaltic pump (Ismatec, Reglo Digital) at a flow rate of 0.1 ml min⁻¹ through a glass reservoir, the capillary, and connecting Teflon tubing (1 mm inner diameter). A far-red laser diode (750 \pm 5 nm, 3 mW, Leading-Tech Laser Co.) was used to transform the sample

to the Pr state by constantly illuminating the sample through the Teflon tubing.

The femtosecond pump–probe technique was used to measure transient absorption spectra with time resolution down to 0.15 ps. Ti:sapphire laser (Libra-F, Coherent Inc.) and optical parametric amplifier (Topas-C, Light Conversion Ltd.) were used to produce pump and probe pulses in the ExciPro (CDP) measurement system as previously described [72]. The OD₇₀₀ of the samples was about 0.45. The 700 \pm 10 nm pump pulse with energy density of 0.026 mJ/cm² was used to excite the CBD-WT, CBD-Y263F and CBD-H260A samples. The transition absorption was measured in the spectral range 530–770 nm.

Fluorescence decays of the samples in the sub-nanosecond and nanosecond time scales were measured using a time-correlated single photon counting (TCSPC) system

consisting of a HydraHarp 400 controller and a PDL 800-B driver (PicoQuant GmbH). The excitation wavelength was 660 nm from a pulsed diode laser head LDH-P-C-660. The repetition rate of the excitation pulses was set to 40 MHz in all measurements, and the output power of the laser was 0.98 mW for 660 nm excitation. The Jobin Yvon mono-chromator was used to detect the emission at 720 nm with a single photon avalanche photodiode (SPAD, MPD-1CTC). The time resolution was approximately 70 ps (full width at half-maximum of the instrument response function, IRF). The data were fitted with multi-exponential functions to obtain fluorescence lifetimes [44]. In addition to the fluorescence decay components, a fast rise component of about 20 ps was needed to obtain satisfactory fits at early time points.

Supplementary Information The online version contains supplementary material available at <https://doi.org/10.1007/s43630-022-00272-6>.

Acknowledgements This work was supported by Academy of Finland grants 285461 (H.T.), 330678 (H.T., J.R.), 277194 (H.L.), and 290677 (S.M.). We acknowledge the European Synchrotron Radiation Facility (ESRF) for providing synchrotron access for crystal data collection. We thank Prof. Janne Ihalainen (University of Jyväskylä) for all the help in all aspects of the paper, Prof. Gerrit Groenhof (University of Jyväskylä) for support, and Prof. Nikolai V. Tkachenko (Tampere University) for help and facilities for time-resolved absorption spectroscopy. We also thank M.Sc. Alli Liukkonen (University of Jyväskylä) and Dr. Heikki Häkkänen (University of Jyväskylä) for the assistance in laboratory and spectroscopy, respectively.

Author contributions HT and HL: conceived the project. HL, JR, SM, SK, and HT: conceived the experiments and analyzed the data. Paper was designed and written by HL, HT, and JR with input from all other authors.

Funding Open Access funding provided by University of Jyväskylä (JYU).

Declarations

Conflict of interest On behalf of all authors, the corresponding author states that there is no conflict of interest.

Open Access This article is licensed under a Creative Commons Attribution 4.0 International License, which permits use, sharing, adaptation, distribution and reproduction in any medium or format, as long as you give appropriate credit to the original author(s) and the source, provide a link to the Creative Commons licence, and indicate if changes were made. The images or other third party material in this article are included in the article's Creative Commons licence, unless indicated otherwise in a credit line to the material. If material is not included in the article's Creative Commons licence and your intended use is not permitted by statutory regulation or exceeds the permitted use, you will need to obtain permission directly from the copyright holder. To view a copy of this licence, visit <http://creativecommons.org/licenses/by/4.0/>.

References

- Butler, W. L., Norris, K. H., Siegelman, H. W., & Hendricks, S. B. (1959). Detection, assay, and preliminary purification of the pigment controlling photoresponsive development of plants. *Proceedings of the National Academy of Sciences*, *45*, 1703–1708. <https://doi.org/10.1073/pnas.45.12.1703>
- Karniol, B., Wagner, J. R., Walker, J. M., & Vierstra, R. D. (2005). Phylogenetic analysis of the phytochrome superfamily reveals distinct microbial subfamilies of photoreceptors. *Biochemical Journal*, *392*, 103–116.
- Bhoo, S. H., Davis, S. J., Walker, J., Karniol, B., & Vierstra, R. D. (2001). Bacteriophytochromes are photochromic histidine kinases using a biliverdin chromophore. *Nature*, *414*, 776–779. <https://doi.org/10.1038/414776a>
- Wagner, J. R., Brunzelle, J. S., Forest, K. T., & Vierstra, R. D. (2005). A light-sensing knot revealed by the structure of the chromophore-binding domain of phytochrome. *Nature*, *438*, 325–331.
- Takala, H., Bjorling, A., Berntsson, O., Lehtivuori, H., Niebling, S., Hoernke, M., et al. (2014). Signal amplification and transduction in phytochrome photosensors. *Nature*, *509*, 245–248. <https://doi.org/10.1038/nature13310>
- Bjorling, A., Berntsson, O., Lehtivuori, H., Takala, H., Hughes, A. J., Panman, M., et al. (2016). Structural photoactivation of a full-length bacterial phytochrome. *SciAdv*, *2*, e1600920. <https://doi.org/10.1126/sciadv.1600920>
- Multamäki, E., Nanekar, R., Morozov, D., Lievonen, T., Golonka, D., Wahlgren, W. Y., et al. (2021). Comparative analysis of two paradigm bacteriophytochromes reveals opposite functionalities in two-component signaling. *Nature Communications*, *12*, 4394. <https://doi.org/10.1038/s41467-021-24676-7>
- Wagner, J. R., Zhang, J., von Stetten, D., Gunther, M., Murgida, D. H., Mroginski, M. A., et al. (2008). Mutational analysis of *Deinococcus radiodurans* bacteriophytochrome reveals key amino acids necessary for the photochromicity and proton exchange cycle of phytochromes. *Journal of Biological Chemistry*, *283*, 12212–12226. <https://doi.org/10.1074/jbc.M709355200>
- Sineshchekov, V. A. (1995). Photobiophysics and photobiochemistry of the heterogeneous phytochrome system. *Biochimica et Biophysica Acta (BBA) Bioenergetics*, *1228*, 125–164. [https://doi.org/10.1016/0005-2728\(94\)00173-3](https://doi.org/10.1016/0005-2728(94)00173-3)
- Song, C., Rohmer, T., Tiersch, M., Zaanen, J., Hughes, J., & Matysik, J. (2013). Solid-state NMR spectroscopy to probe photoactivation in canonical phytochromes. *Photochemistry and Photobiology*, *89*, 259–273. <https://doi.org/10.1111/php.12029>
- Takala, H., Edlund, P., Ihalainen, J. A., & Westenhoff, S. (2020). Tips and turns of bacteriophytochrome photoactivation. *Photochemical and Photobiological Sciences*. <https://doi.org/10.1039/D0PP00117A>
- Dasgupta, J., Frontiera, R. R., Taylor, K. C., Lagarias, J. C., & Mathies, R. A. (2009). Ultrafast excited-state isomerization in phytochrome revealed by femtosecond stimulated Raman spectroscopy. *Proceedings of the National Academy of Sciences USA*, *106*, 1784–1789. <https://doi.org/10.1073/pnas.0812056106>
- Toh, K. C., Stojkovic, E. A., van Stokkum, I. H., Moffat, K., & Kennis, J. T. (2010). Proton-transfer and hydrogen-bond interactions determine fluorescence quantum yield and photochemical efficiency of bacteriophytochrome. *Proceedings of the National Academy of Sciences USA*, *107*, 9170–9175. <https://doi.org/10.1073/pnas.0911535107>
- Ihalainen, J. A., Takala, H., & Lehtivuori, H. (2015). Fast photochemistry of prototypical phytochromes-A species vs. subunit

- specific comparison. *Frontiers in Molecular Biosciences*, 2, 75. <https://doi.org/10.3389/fmolb.2015.00075>
15. Mathes, T., Ravensbergen, J., Kloz, M., Gleichmann, T., Gallagher, K. D., Woitowich, N. C., et al. (2015). Femto- to microsecond photodynamics of an unusual bacteriophytochrome. *The Journal of Physical Chemistry Letters*, 6, 239–243. <https://doi.org/10.1021/jz502408n>
 16. Velazquez Escobar, F., Kneip, C., Michael, N., Hildebrandt, T., Tavraz, N., Gärtner, W., et al. (2020). The lumi-R intermediates of prototypical phytochromes. *The Journal of Physical Chemistry B*, 124, 4044–4055. <https://doi.org/10.1021/acs.jpcc.0c01059>
 17. Kübel, J., Chenhiliyan, M., Ooi, S. A., Gustavsson, E., Isaksson, L., Kuznetsova, V., et al. (2020). Transient IR spectroscopy identifies key interactions and unravels new intermediates in the photocycle of a bacterial phytochrome. *Physical Chemistry Chemical Physics*, 22, 9195–9203. <https://doi.org/10.1039/C9CP06995J>
 18. Edlund, P., Takala, H., Claesson, E., Henry, L., Dods, R., Lehtivuori, H., et al. (2016). The room temperature crystal structure of a bacterial phytochrome determined by serial femtosecond crystallography. *Scientific Reports*, 6, 35279. <https://doi.org/10.1038/srep35279>
 19. Wagner, J. R., Zhang, J., Brunzelle, J. S., Vierstra, R. D., & Forest, K. T. (2007). High resolution structure of Deinococcus bacteriophytochrome yields new insights into phytochrome architecture and evolution. *Journal of Biological Chemistry*, 282, 12298–12309.
 20. Burgie, E. S., Wang, T., Bussell, A. N., Walker, J. M., Li, H., & Vierstra, R. D. (2014). Crystallographic and electron microscopic analyses of a bacterial phytochrome reveal local and global rearrangements during photoconversion. *Journal of Biological Chemistry*, 289, 24573–24587. <https://doi.org/10.1074/jbc.M114.571661>
 21. Takala, H., Lehtivuori, H. K., Berntsson, O., Hughes, A., Nanekar, R., Niebling, S., et al. (2018). On the (un)coupling of the chromophore, tongue interactions, and overall conformation in a bacterial phytochrome. *Journal of Biological Chemistry*, 293, 8161–8172. <https://doi.org/10.1074/jbc.RA118.001794>
 22. Song, C., Psakis, G., Lang, C., Mailliet, J., Gärtner, W., Hughes, J., et al. (2011). Two ground state isoforms and a chromophore D-ring photoflip triggering extensive intramolecular changes in a canonical phytochrome. *Proceedings of the National Academy of Sciences USA*, 108, 3842–3847. <https://doi.org/10.1073/pnas.1013377108>
 23. Velazquez Escobar, F., Lang, C., Takiden, A., Schneider, C., Balke, J., Hughes, J., et al. (2017). Protonation-dependent structural heterogeneity in the chromophore binding site of cyanobacterial phytochrome Cph1. *The Journal of Physical Chemistry B*, 121, 47–57. <https://doi.org/10.1021/acs.jpcc.6b09600>
 24. Kirpich, J. S., Mix, L. T., Martin, S. S., Rockwell, N. C., Lagarias, J. C., & Larsen, D. S. (2018). Protonation heterogeneity modulates the ultrafast photocycle initiation dynamics of phytochrome Cph1. *Journal of Physical Chemistry Letters*, 9, 3454–3462. <https://doi.org/10.1021/acs.jpcclett.8b01133>
 25. Woitowich, N. C., Halavaty, A. S., Waltz, P., Kupitz, C., Valera, J., Tracy, G., et al. (2018). Structural basis for light control of cell development revealed by crystal structures of a myxobacterial phytochrome. *IUCrJ*, 5, 619–634. <https://doi.org/10.1107/S2052252518010631>
 26. Kraskov, A., Buhrke, D., Scheerer, P., Shaef, I., Sanchez, J. C., Carrillo, M., et al. (2021). On the role of the conserved histidine at the chromophore isomerization site in phytochromes. *The Journal of Physical Chemistry B*, 125, 13696–13709. <https://doi.org/10.1021/acs.jpcc.1c08245>
 27. Claesson, E., Wahlgren, W. Y., Takala, H., Pandey, S., Castillon, L., Kuznetsova, V., et al. (2020). The primary structural photoresponse of phytochrome proteins captured by a femto-second X-ray laser. *eLife*. <https://doi.org/10.7554/eLife.53514>
 28. Lenngren, N., Edlund, P., Takala, H., Stucki-Buchli, B., Rumpf, J., Peshev, I., et al. (2018). Coordination of the biliverdin D-ring in bacteriophytochromes. *Physical Chemistry Chemical Physics*, 20, 18216–18225. <https://doi.org/10.1039/c8cp01696h>
 29. Cho-Shuen, H., Kramer, C. R., Masanari, O., Backus Ellen, H. G., Yuki, N., & Mischa, B. (2013). Mechanism of vibrational energy dissipation of free OH groups at the air–water interface. *Proceedings of the National Academy of Sciences*, 110, 18780–18785. <https://doi.org/10.1073/pnas.1314770110>
 30. Hochreiter, B., Pardo-Garcia, A., & Schmid, J. A. (2015). Fluorescent proteins as genetically encoded FRET biosensors in life sciences. *Sensors*. <https://doi.org/10.3390/s151026281>
 31. Lehtivuori, H., Bhattacharya, S., Angenent-Mari, N. M., Satyshur, K. A., & Forest, K. T. (2015). Removal of chromophore-proximal polar atoms decreases water content and increases fluorescence in a near infrared phytofluor. *Frontiers in Molecular Biosciences*, 2, 65. <https://doi.org/10.3389/fmolb.2015.00065>
 32. Shu, X., Royant, A., Lin, M. Z., Aguilera, T. A., Lev-Ram, V., Steinbach, P. A., et al. (2009). Mammalian expression of infrared fluorescent proteins engineered from a bacterial phytochrome. *Science*, 324, 804–807. <https://doi.org/10.1126/science.1168683>
 33. Auldridge, M. E., Satyshur, K. A., Anstrom, D. M., & Forest, K. T. (2012). Structure-guided engineering enhances a phytochrome-based infrared fluorescent protein. *Journal of Biological Chemistry*, 287, 7000–7009. <https://doi.org/10.1074/jbc.M111.295121>
 34. Yu, D., Gustafson, W. C., Han, C., Lafaye, C., Noirclerc-Savoye, M., Ge, W. P., et al. (2014). An improved monomeric infrared fluorescent protein for neuronal and tumour brain imaging. *Nature Communications*, 5, 3626. <https://doi.org/10.1038/ncomms4626>
 35. Bhattacharya, S., Auldridge, M. E., Lehtivuori, H., Ihala, J. A., & Forest, K. T. (2014). Origins of fluorescence in evolved bacteriophytochromes. *Journal of Biological Chemistry*, 289, 32144–32152. <https://doi.org/10.1074/jbc.M114.589739>
 36. Filonov, G. S., Piatkevich, K. D., Ting, L. M., Zhang, J., Kim, K., & Verkhusha, V. V. (2011). Bright and stable near-infrared fluorescent protein for in vivo imaging. *Nature Biotechnology*, 29, 757–761. <https://doi.org/10.1038/nbt.1918>
 37. Shcherbakova, D. M., Baloban, M., Emelyanov, A. V., Brenowitz, M., Guo, P., & Verkhusha, V. V. (2016). Bright monomeric near-infrared fluorescent proteins as tags and biosensors for multiscale imaging. *Nature Communications*, 7, 12405. <https://doi.org/10.1038/ncomms12405>
 38. Piatkevich, K. D., Subach, F. V., & Verkhusha, V. V. (2013). Far-red light photoactivatable near-infrared fluorescent proteins engineered from a bacterial phytochrome. *Nature Communications*, 4, 2153. <https://doi.org/10.1038/ncomms3153>
 39. Shcherbakova, D. M., Baloban, M., & Verkhusha, V. V. (2015). Near-infrared fluorescent proteins engineered from bacterial phytochromes. *Current Opinion in Chemical Biology*, 27, 52–63. <https://doi.org/10.1016/j.cbpa.2015.06.005>
 40. Fischer, A. J., & Lagarias, J. C. (2004). Harnessing phytochrome's glowing potential. *Proceedings of the National Academy of Sciences USA*, 101, 17334–17339.
 41. Rodriguez, E. A., Tran, G. N., Gross, L. A., Crisp, J. L., Shu, X., Lin, J. Y., et al. (2016). A far-red fluorescent protein evolved from a cyanobacterial phycobiliprotein. *Nature Methods*, 13, 763–769. <https://doi.org/10.1038/nmeth.3935>
 42. Nagano, S., Sadeghi, M., Balke, J., Fleck, M., Heckmann, N., Psakis, G., et al. (2022). Improved fluorescent phytochromes for in situ imaging. *Scientific Reports*, 12, 5587. <https://doi.org/10.1038/s41598-022-09169-x>
 43. Baloban, M., Shcherbakova, D. M., Pletnev, S., Pletnev, V. Z., Lagarias, J. C., & Verkhusha, V. V. (2017). Designing brighter near-infrared fluorescent proteins: insights from structural and

- biochemical studies. *Chemical Science*, 8, 4546–4557. <https://doi.org/10.1039/c7sc00855d>
44. Lehtivuori, H., Rissanen, I., Takala, H., Bamford, J., Tkachenko, N. V., & Ihalainen, J. A. (2013). Fluorescence properties of the chromophore-binding domain of bacteriophytochrome from *Deinococcus radiodurans*. *The Journal of Physical Chemistry B*, 117, 11049–11057. <https://doi.org/10.1021/jp312061b>
 45. Ulijasz, A. T., Cornilescu, G., von Stetten, D., Kaminski, S., Mroginski, M. A., Zhang, J., et al. (2008). Characterization of two thermostable cyanobacterial phytochromes reveals global movements in the chromophore-binding domain during photoconversion. *Journal of Biological Chemistry*, 283, 21251–21266. <https://doi.org/10.1074/jbc.M801592200>
 46. Velazquez Escobar, F., Hildebrandt, T., Utesch, T., Schmitt, F. J., Seuffert, I., Michael, N., et al. (2014). Structural parameters controlling the fluorescence properties of phytochromes. *Biochemistry*, 53, 20–29. <https://doi.org/10.1021/bi401287u>
 47. Li, F., Burgie, E. S., Yu, T., Heroux, A., Schatz, G. C., Vierstra, R. D., et al. (2015). X-ray radiation induces deprotonation of the bilin chromophore in crystalline *D. radiodurans* phytochrome. *Journal of the American Chemical Society*, 137, 2792–2795. <https://doi.org/10.1021/ja510923m>
 48. Feliks, M., Lafaye, C., Shu, X., Royant, A., & Field, M. (2016). Structural determinants of improved fluorescence in a family of bacteriophytochrome-based infrared fluorescent proteins: insights from continuum electrostatic calculations and molecular dynamics simulations. *Biochemistry*, 55, 4263–4274. <https://doi.org/10.1021/acs.biochem.6b00295>
 49. Modi, V., Donnini, S., Groenhof, G., & Morozov, D. (2019). Protonation of the biliverdin IX α chromophore in the red and far-red photoactive states of a bacteriophytochrome. *The Journal of Physical Chemistry B*, 123, 2325–2334. <https://doi.org/10.1021/acs.jpcc.9b01117>
 50. von Stetten, D., Seibeck, S., Michael, N., Scheerer, P., Mroginski, M. A., Murgida, D. H., et al. (2007). Highly conserved residues Asp-197 and His-250 in Agp1 phytochrome control the proton affinity of the chromophore and Pfr formation. *Journal of Biological Chemistry*, 282, 2116–2123. <https://doi.org/10.1074/jbc.M608878200>
 51. Zienicke, B., Molina, I., Glenz, R., Singer, P., Ehmer, D., Escobar, F. V., et al. (2013). Unusual spectral properties of bacteriophytochrome Agp2 result from a deprotonation of the chromophore in the red-absorbing form Pr. *Journal of Biological Chemistry*, 288, 31738–31751. <https://doi.org/10.1074/jbc.M113.479535>
 52. Rumfeldt, J. A., Takala, H., Liukkonen, A., & Ihalainen, J. A. (2019). UV-Vis spectroscopy reveals a correlation between Y263 and BV protonation states in bacteriophytochromes. *Photochemistry and Photobiology*, 95, 969–979. <https://doi.org/10.1111/php.13095>
 53. Shang, L., Rockwell, N. C., Martin, S. S., & Lagarias, J. C. (2010). Biliverdin amides reveal roles for propionate side chains in bilin reductase recognition and in holophytochrome assembly and photoconversion. *Biochemistry*, 49, 6070–6082. <https://doi.org/10.1021/bi100756x>
 54. Fischer, T., van Wilderen, L. J. G. W., Gnau, P., Bredenbeck, J., Essen, L.-O., Wachtveitl, J., et al. (2021). Ultrafast photoconversion dynamics of the knotless phytochrome SynCph2. *International Journal of Molecular Sciences*. <https://doi.org/10.3390/ijms221910690>
 55. van Thor, J. J., Borucki, B., Crielaard, W., Otto, H., Lamparter, T., Hughes, J., et al. (2001). Light-induced proton release and proton uptake reactions in the cyanobacterial phytochrome Cph1. *Biochemistry*, 40, 11460–11471.
 56. Yuu, H., Rockwell, N. C., Kaori, N., Rei, N., Yutaka, U., Katsuhiko, I., et al. (2013). Green/red cyanobacteriochromes regulate complementary chromatic acclimation via a protochromic photocycle. *Proceedings of the National Academy of Sciences*, 110, 4974–4979. <https://doi.org/10.1073/pnas.1302909110>
 57. Wang, D., Qin, Y., Zhang, M., Li, X., Wang, L., Yang, X., et al. (2020). The origin of ultrafast multiphasic dynamics in photoisomerization of bacteriophytochrome. *The Journal of Physical Chemistry Letters*, 11, 5913–5919. <https://doi.org/10.1021/acs.jpcclett.0c01394>
 58. Heyne, K., Herbst, J., Stehlik, D., Esteban, B., Lamparter, T., Hughes, J., et al. (2002). Ultrafast dynamics of phytochrome from the cyanobacterium *Synechocystis*, reconstituted with phycocyanobilin and phycoerythrobilin. *Biophysical Journal*, 82, 1004–1016. [https://doi.org/10.1016/S0006-3495\(02\)75460-X](https://doi.org/10.1016/S0006-3495(02)75460-X)
 59. Müller, M. G., Lindner, I., Martin, I., Gärtner, W., & Holzwarth, A. R. (2008). Femtosecond kinetics of photoconversion of the higher plant photoreceptor phytochrome carrying native and modified chromophores. *Biophysical Journal*, 94, 4370–4382. <https://doi.org/10.1529/biophysj.106.091652>
 60. Kim, P. W., Rockwell, N. C., Martin, S. S., Lagarias, J. C., & Larsen, D. S. (2014). Dynamic inhomogeneity in the photodynamics of cyanobacterial phytochrome Cph1. *Biochemistry*, 53, 2818–2826. <https://doi.org/10.1021/bi500108s>
 61. Carrillo, M., Pandey, S., Sanchez, J., Noda, M., Poudyal, I., Aldama, L., et al. (2021). High-resolution crystal structures of transient intermediates in the phytochrome photocycle. *Structure*, 29, 743–754.e4. <https://doi.org/10.1016/j.str.2021.03.004>
 62. Ihalainen, J. A., Gustavsson, E., Schroeder, L., Donnini, S., Lehtivuori, H., Isaksson, L., et al. (2018). Chromophore-protein interplay during the phytochrome photocycle revealed by step-scan FTIR spectroscopy. *Journal of the American Chemical Society*, 140, 12396–12404. <https://doi.org/10.1021/jacs.8b04659>
 63. Voltz, K., Léonard, J., Touceda, P. T., Conyard, J., Chaker, Z., Dejaegere, A., et al. (2016). Quantitative sampling of conformational heterogeneity of a DNA hairpin using molecular dynamics simulations and ultrafast fluorescence spectroscopy. *Nucleic Acids Research*, 44, 3408–3419. <https://doi.org/10.1093/nar/gkw077>
 64. Sineshchekov, V. A., & Bekasova, O. D. (2020). Two distinct photoprocesses in cyanobacterial bilin pigments: energy migration in light-harvesting phycobiliproteins versus photoisomerization in phytochromes. *Photochemistry and Photobiology*, 96, 750–767. <https://doi.org/10.1111/php.13197>
 65. Schmidt, P., Gertsch, T., Remberg, A., Gärtner, W., Braslavsky, S. E., & Schaffner, K. (1998). The complexity of the Pr to Pfr phototransformation kinetics is an intrinsic property of native phytochrome. *Photochemistry and Photobiology*, 68, 754–761. <https://doi.org/10.1111/j.1751-1097.1998.tb02541.x>
 66. Nieder, J. B., Brecht, M., & Bittl, R. (2009). Dynamic intracomplex heterogeneity of phytochrome. *Journal of American Chemical Society*, 131, 69–71. <https://doi.org/10.1021/ja8058292>
 67. von Stetten, D., Gunther, M., Scheerer, P., Murgida, D. H., Mroginski, M. A., Krauss, N., et al. (2008). Chromophore heterogeneity and photoconversion in phytochrome crystals and solution studied by resonance Raman spectroscopy. *Angewandte Chemie International Edition England*, 47, 4753–4755. <https://doi.org/10.1002/anie.200705716>
 68. Kabsch, W. (2010). Xds. *Acta Crystallographica Section D Biological Crystallography*, 66, 125–132. <https://doi.org/10.1107/S0907444909047337>
 69. Karplus, P. A., & Diederichs, K. (2012). Linking crystallographic model and data quality. *Science*, 336, 1030–1033. <https://doi.org/10.1126/science.1218231>
 70. McCoy, A. J., Grosse-Kunstleve, R. W., Adams, P. D., Winn, M. D., Storoni, L. C., & Read, R. J. (2007). Phaser crystallographic software. *Journal of Applied Crystallography*, 40, 658–674. <https://doi.org/10.1107/S0021889807021206>
 71. Murshudov, G. N., Skubák, P., Lebedev, A. A., Pannu, N. S., Steiner, R. A., Nicholls, R. A., et al. (2011). REFMAC5 for the

- refinement of macromolecular crystal structures. *Acta Crystallographica Section D Biological Crystallography*, 67, 355–367. <https://doi.org/10.1107/S0907444911001314>
72. Sirbu, D., Turta, C., Benniston, A. C., Abou-Chahine, F., Lemmetyinen, H., Tkachenko, N. V., et al. (2014). Synthesis and

properties of a meso- tris-ferrocene appended zinc(ii) porphyrin and a critical evaluation of its dye sensitised solar cell (DSSC) performance. *RSC Advances*, 4, 22733–22742. <https://doi.org/10.1039/C4RA03105A>

Authors and Affiliations

Heli Lehtivuori^{1,2}  · Jessica Rumfeldt³  · Satu Mustalahti⁴  · Sami Kurkinen^{3,5}  · Heikki Takala^{3,6} 

¹ Nanoscience Center, Department of Physics, University of Jyväskylä, 40014 Jyväskylä, Finland

² Research and Innovation Services, Tampere University, 33014 Tampere, Finland

³ Nanoscience Center, Department of Biological and Environmental Sciences, University of Jyväskylä, 40014 Jyväskylä, Finland

⁴ Nanoscience Center, Department of Chemistry, University of Jyväskylä, 40014 Jyväskylä, Finland

⁵ Institute of Biomedicine, Integrative Physiology and Pharmacy, University of Turku, 20014 Turku, Finland

⁶ Department of Anatomy, Faculty of Medicine, University of Helsinki, Box 63, 00014 Helsinki, Finland